A consistent mass-conserving C-staggered method for shallow water equations on global reduced grids

Genilson S. Lima, Pedro S. Peixoto
Instituto de Matemática e Estatistica, Universidade de São Paulo, Brazil
genilson@ime.usp.br; pedrosp@ime.usp.br

March, 2022

A consistent mass-conserving C-staggered method for shallow water equations on global reduced grids

Genilson S. Lima*, Pedro S. Peixoto

Instituto de Matemática e Estatistica, Universidade de São Paulo, R. do Matão 1010, São Paulo, 05508-090, Brazil

ARTICLE INFO

Keywords:
global reduced grids
finite differences
finite volumes
shallow-water equations
conservation
consistency

ABSTRACT

The increasing number of cores in modern supercomputers motivated the search for methods with better scalability to model the atmospheric dynamics in global weather forecasting and climate simulations. This objective renewed the interest in grid-point schemes with quasi-uniform spherical grids, with each alternative providing some good properties and some disadvantages. Here, we target reduced latitude-longitude global grids, and build from derivations of previous schemes trying to circumvent existing limitations. A method is proposed for the shallow water equations on a C-staggered global reduced grid using a combination of finite differences, finite volumes, and explicit time-stepping. This scheme applies trigonometric approximations, has some conservative properties, and uses numerically consistent operators everywhere. Classical and recently proposed benchmarks were used to evaluate convergence, stability, and accumulation of errors. Results indicated that the trigonometric scheme is a good candidate for global models, providing adequate accuracy at reasonable computational cost and suitability for parallel processing.

1. Introduction

Since some decades ago, the growth in computational capacity on processing servers has been related to the use of a larger number of cores. To explore this growing capacity properly in global numerical weather prediction models, we need numerical methods with better computational scalability to model the atmospheric dynamics (Williamson, 2007). Calculations with global dependency, or grids with strong accumulation of points, lead to potential communication bottlenecks in parallel processing, and explicit grid-point methods with quasi-uniform spherical grids are one alternative to avoid such problems. Unfortunately, due to grid irregularities, many schemes can yield low accuracy, instabilities, accumulation of errors, or short-wavelength (grid-related) errors (Staniforth and Thuburn, 2012; Williamson, 2007).

Full latitude-longitude grids have symmetrical cells, but with a strong concentration of points in polar regions (the often-called "pole-problem"). Reduced global grids with logically rectangular cells are one alternative for spherical quasi-uniform grids. They have cells defined on constant latitude levels, but reduce the number of cells in the proximity of polar regions. Edges are segments of latitude, or longitude, lines, and points are zonally aligned, therefore resulting in symmetrical cells. Transition lines, when the number of cells is reduced from one latitude circle to the next, require interpolations of fields, and this is the main concern when using such reduced global grids. However, due to the zonal distributions of cells, purpose specific interpolations can be derived making use of local one-dimensional approximation.

Gates, Riegel, Kurihara, and Holloway were the first ones to employ reduced global grids (Gates and Riegel, 1962; Kurihara, 1965; Kurihara and Holloway Jr, 1967). They obtained global methods with a timestep limitation (due to CFL constraint) similar in any region of the grid, avoiding the overwhelming timestep restriction imposed by regular latitude-longitude global grids. However, simulations indicated an accumulation of error in transition lines and polar regions. Dey (1969) and Shuman (1970) showed that this polar error was related to lack of consistency of operators at the poles, that is, some operators have an error that does not decrease when the grid resolution is higher (the "pole-problem" on reduced grids). The polynomial-discrete divergence was consistent only with completely regular latitude-longitude grids. Purser (1988) presented an alternative way to calculate interpolations and finite differences on reduced grids, showing that trigonometric functions can be used to provide consistent approximations.

genilson@ime.usp.br (G.S. Lima); pedrosp@ime.usp.br (P.S. Peixoto)
ORCID(s): 0000-0002-9635-2048 (G.S. Lima); 0000-0003-2358-3221 (P.S. Peixoto)

Numerical methods for global reduced grids were left aside for some period in the literature, until they regained interest due to the computational requirements of modern supercomputers. Recent studies usually give special attention to polar regions, for instance, employing different approximations or a more expensive filter. Some options lead to approximations with higher consistency order, and others provide methods with some conservative properties. Starius (2014) employed polynomial approximations on geodesic lines crossing the cells, therefore using more points for auxiliary calculations. Li (2018) studied a scheme with mixed A, C, and D staggering and an auxiliary representation for polar regions. Bénard and Glinton (2019) employed trigonometric approximations for interpolations and derivatives with A-grid (non-staggered) schemes and a complete Fourier filter in polar regions (to control computational polar modes). More recently, Goyman and Shashkin (2021) showed an alternative method for global reduced grids preserving conservative properties with finite differences and polynomial approximations, but worked on a linearized model only. Therefore, we note that the task of deriving accurate and stable schemes for reduced global grids for nonlinear horizontal dynamics, that present some mimetic properties, such as conservation of mass, is still a subject of open concerns.

Since the early days of the development of numerical methods for atmosphere dynamics, there has been a concern in ensuring that numerical methods mimic some properties of the continuous problem. For instance, Arakawa (1966) showed that conservative properties could prevent nonlinear numerical instability. Winninghoff studied the effects of different staggering options (Winninghoff, 1968; Mesinger and Arakawa, 1976), indicating that a C-staggering could provide a better representation of gravity waves. These results were later confirmed and expanded on, showing methods with several conservative properties and consistent approximations on latitude-longitude C-staggered grids (Sadourny, 1975; Burridge and Haseler, 1977; Arakawa and Lamb, 1981).

With the re-interest in quasi-uniform grids, several finite volume or finite difference methods with conservation properties were proposed for unstructured (mostly triangular or Voronoi) grids. These schemes are derived for grids with no "hanging nodes", that is, the transition between one cell and a neighbor cell is precisely defined by a single edge, that only belong to these two cells. Therefore, on such grids, there is no need for transition lines with interpolations, but they rely on more complex geometry dependent stencils. For instance, Ringler et al. (2010) studied a method with several mimetic properties on C-staggered Voronoi grids, ensuring mass and energy conservation, as well as other properties of interest for atmosphere dynamics. This scheme is general and may be used on arbitrary unstructured grids, however, two of the proposed approximations can be non-consistent (which halt convergence of the overall scheme), and the grid may amplify the errors in some regions (Weller et al., 2012; Peixoto and Barros, 2013; Peixoto, 2016). This method will be referred to as TRSK hereafter. Peixoto, Eldred, and Randall showed schemes for different grids with more consistency (Peixoto (2016)) or more conservative properties (Eldred (2015); Eldred and Randall (2017)). Nevertheless, these alternatives can be less stable, or less accurate, than TRSK.

As noted, employing different options, one can obtain methods with some distinct good properties and also some issues. While Sadourny uses C-staggered regular global grids, with consistent approximations and several mimetic properties, it is not adequate for parallel processing. On the other hand, TRSK works with C-staggered Voronoi grids and has many conservative properties but some operators are non-consistent and the simulations indicate grid-imprinting errors. Bénard and Glinton use A-non-staggered reduced grids and objects with a high order of consistency but they do not have conservation and simulations show some short-wavelength errors.

The target of this paper is to make use of the regularity and symmetries of the reduced global grids, adapt existing techniques derived for other schemes, and propose a method adequate for parallel processing and that can provide accurate and stable solutions. Derivations will be restricted to schemes for shallow water equations on C-staggered global reduced grids using finite differences, finite volumes, and explicit time-step. We will describe conditions to achieve consistency and some conservation properties, explore characteristics of alignment and symmetry, and propose a method.

The presented method is an adaptation considering the scheme of Bénard and Glinton and results from TRSK. It calculates trigonometric approximations for interpolations, uses finite differences and finite volumes, mass is preserved, and the operators are consistent everywhere. No special grids are required for the poles. This scheme employs new expressions to some approximations. Numerical tests will be applied to check convergence, stability, grid-imprinting, and other short-wavelength errors. Overall, the trigonometric scheme has good results as a global method.

We organized this paper as follows. Section 2 describes the equations, grids, and notations. Section 3 presents some results about consistency and conservation with reduced grids. Sections 4 exhibit the method and its numerical tests.

2. Continuous and discrete framework

2.1. Shallow water Equations on the sphere

We will consider the shallow water equations on a sphere as a simplified model for geophysical fluids, in particular as a representation of barotropic dynamics of the atmosphere. This model describes a two-dimensional fluid layer moving under the influence of gravity, rotation, and topography. The fluid is assumed incompressible and the flow is barotropic and hydrostatic (Vallis, 2006; Pedlosky et al., 1987). There are different ways to represent these equations (Williamson et al., 1992). Here, we use the vector-invariant form, as it is known to help in the derivation of methods with energy conservation properties (Sadourny (1975); Arakawa and Lamb (1981); Ringler et al. (2010)).

In the continuous problem, each function is defined on the entire sphere. Coordinates are latitude $\varphi \in [-\pi/2, \pi/2]$, longitude $\lambda \in [-\pi, \pi]$, and time instant t. At each point, we have the reference vectors pointing eastward, $\vec{i}(\lambda, \varphi)$, northward, $\vec{j}(\lambda, \varphi)$, and radially with respect to the sphere (height), $\vec{k}(\lambda, \varphi)$. The reference spherical radius, a, gravity acceleration, g, and rotation angular velocity, Ω, are constants. Topography, $b(\lambda, \varphi)$, is a given function. Horizontal Coriolis function is $f(\varphi) = 2\Omega \sin \varphi$. Main prognostic variables are the layer thickness, $h(\lambda, \varphi, t)$, zonal component of wind, $u(\lambda, \varphi, t)$, and meridional wind component, $v(\lambda, \varphi, t)$. Auxiliary functions are the relative vorticity, $\zeta = \vec{k} \cdot \nabla \times \vec{u}$, absolute vorticity, $\xi = \zeta + f$, potential vorticity, $q = (\zeta + f)/h$, kinetic energy, $K = \vec{u} \cdot \vec{u}/2$, and geopotential, $\Phi = g(h + b)$.

We wish to determine $h(\lambda, \varphi, t)$, $u(\lambda, \varphi, t)$ and $v(\lambda, \varphi, t)$ satisfying an initial condition and the following differential equations,

$$\partial_t h = -\nabla \cdot h\vec{u}, \tag{1}$$

$$\partial_t u = +(\zeta + f)v - \partial_x(K + \Phi), \tag{2}$$

$$\partial_t v = -(\zeta + f)u - \partial_y(K + \Phi), \tag{3}$$

where, horizontal divergence, vorticity and gradient operators are here written as $\nabla \cdot \vec{u} = (\partial_\lambda u + \partial_\varphi(v \cos\varphi))/(a \cos\varphi)$, $\vec{k} \cdot \nabla \times \vec{u} = (\partial_\lambda v - \partial_\varphi(u \cos\varphi))/(a \cos\varphi)$, $\partial_x h = \partial_\lambda h/(a \cos\varphi)$, and $\partial_y h = \partial_\varphi h/a$. Partial derivatives for coordinates λ, φ, and t are written, respectively, as ∂_λ, ∂_φ, and ∂_t.

2.2. Semi-discrete problem

In the semi-discrete problem, we may consider a different set of points on the sphere for each prognostic variable, defining a "staggered" grid for the variables (Mesinger and Arakawa (1976); Sadourny (1975); Arakawa and Lamb (1981); Ringler et al. (2010)). We will denote the points as X_i, X_e and X_n, respectively corresponding to the positions of the variables at grid points, $h_i(t)$, $u_e(t)$ and $v_n(t)$.

We wish to find grid related time functions $h_i(t)$, $u_e(t)$ and $v_n(t)$ satisfying a discrete initial condition and the following large system of equations,

$$\partial_t h_i = -[\nabla \cdot h\vec{u}]_i, \tag{4}$$

$$\partial_t u_e = +[(\zeta + f)v]_e - [\partial_x(K + \Phi)]_e, \tag{5}$$

$$\partial_t v_n = -[(\zeta + f)u]_n - [\partial_y(K + \Phi)]_n. \tag{6}$$

The operators between square brackets are discrete approximations, yet to be defined. Every object with the same index group (i, e, or n) is related to the same set of points.

To obtain a fully discrete problem, we can apply a temporal numerical scheme to this system of ordinary differential equations. To ensure adequate conditions for parallel processing, we will use explicit time-step and local spatial stencils (using a limited number of neighbors in the discrete operators). Since we will work on a quasi-uniform grid, the explicit time-stepping allows reasonable time step sizes.

The subsequent topics present the grid, position of variables, and the temporal stepping scheme.

2.3. Reduced global grid

There are different options for global quasi-uniform grids (Staniforth and Thuburn (2012), Weller et al. (2012)). Icosahedral grids and cubed sphere grids can be built without hanging nodes, and therefore may avoid transition layers and extra interpolations. However, some cells are not symmetric or badly aligned, that is, they tend to be more deformed and suffer strong grid-imprinting (Peixoto and Barros, 2013; Weller et al., 2012). Reduced grids with rectangular cells

require interpolations at transition lines, however, the points are zonally aligned, and the cells are symmetric. We will consider reduced global grids in order to explore their geometrical properties.

We have essentially two alternatives for transition lines in reduced grids. Using a variable factor, the change in cell size is smooth (Kurihara (1965); Bénard and Glinton (2019)). However, the interpolations have to be described for many situations. Employing a constant rate, the change in size may be less smooth (Purser (1988); Starius (2014); Li (2018)). Nevertheless, the interpolations are related to specific symmetrical configurations. Here, we will apply reductions with factor 2 to benefit from their implied symmetries.

The polar points can be usually taken to be a cell vertex or a cell midpoint. Thuburn and Staniforth (2004) studied these options for regular latitude-longitude grids, and concluded that placing a vertex at polar points may help in the achievement of mimetic properties. The amount of neighbor cells of the polar points also play an important role in the discretization scheme. Dey (1969) showed that better results are achieved using 12 polar cells than considering only 4. Bénard and Glinton (2019) employed 18 cells around each pole. IFS (ECMWF) octahedral reduced grids use 20 polar cells Malardel et al. (2016). We will adopt 16 in this work.

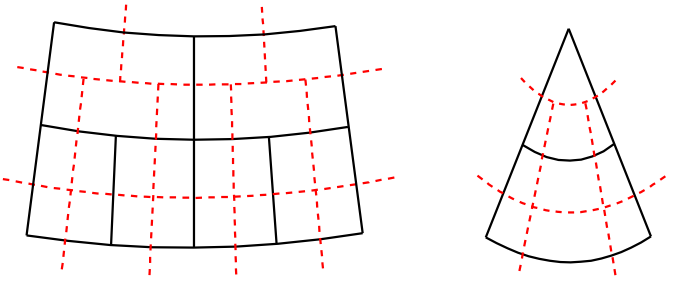

Figure 1: Primal edges (black continuous lines) and dual edges (red dashed lines) at a reduction row (left) and around the polar point (right). Each cell is a latitude-longitude rectangle.

Consider a given number of latitude rows, N, and a uniform meridional angular distance, $\Delta\varphi = \pi/N$. The main (primal) grid will have N rows. There will be a vertex at each polar point (see Figure 1). Cells at each row will have the same angular distances, $\Delta\varphi$, $\Delta\lambda$, and the same central metric distances Δy, Δx (zonal distance between two consecutive centers or meridional distance between North and South edges of a cell). There will be sixteen cells around the polar points. Transitions occur with a factor of 2. They are chosen to keep the ratio $\Delta x/\Delta y$ between 4/3 and 2/3. Edges are segments of latitude or longitude curves. Neighbor primal rows have several meridional edges at the same longitude coordinates.

A dual grid will be defined to have $N-1$ rows and one extra cell around each polar point. Primal and dual zonal curves have an angular distance $\Delta\varphi/2$ from each other. At uniform regions, primal and dual meridional curves have a distance $\Delta\lambda/2$ (See Figure 1).

When we multiply the total number of rows by 2, a new transition line is created closer to the polar points. Other transitions remain almost at the same latitude in both grid resolutions. The zonal angular distance, $\Delta\lambda$, decreases with a factor 1/2 outside the polar areas. In the polar regions, the zonal angular distance remains $\Delta\lambda = 2\pi/16$. Maximum and minimum metric distances decrease with factor 1/2. When the number of rows is a power of 2, the first transition line occurs near to 45^o. Figure 2 shows a section of the grid with $N = 32$ and $N = 64$ (N is the number of rows from the south pole until the north pole).

2.4. Variable grid staggering

Winninghoff compared different alternatives for variable positions at grid cells (Winninghoff, 1968; Mesinger and Arakawa, 1976). A C-staggered grid, with normal velocities at the cell faces and scalar pressure/height at cell centers, allow better representation of the propagation of gravity waves. In C-staggered grids, we can define the cell borders (edges) and cell centers in essentially two ways: (i) assuming edges to be the zonal/meridional lines and the center to be the midpoint of the longitudes and latitudes of the grid box; (ii) using geodesic lines connecting the cell box corners for the edges and assuming the cell mass centroid as center. The former positioning provide better symmetries when building discrete operators, whereas the latter ensures better accuracy in the representation of certain operators related

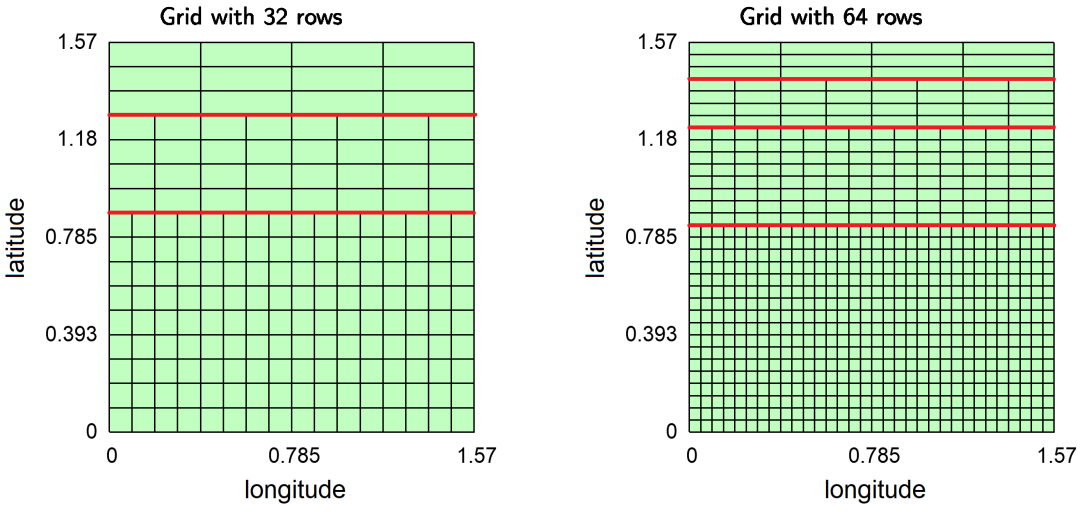

Figure 2: One spherical octant with grids 32 (left) and 64 (right). Red lines indicate the transitions. When the total number of rows is a power of 2, the first transition occurs at approximately 45°, the second is close to 70°, and others are above 80°.

to finite difference and finite volume discretizations. Here, we will follow a C-staggering with latitude-longitude based edge and midpoints layout, in order to make use of the implied symmetry properties.

We will consider four sets of points for variable positioning. The midpoint of a meridional or zonal primal edge is written as X_e (for East or West boundaries of a cell) or X_n (for North or South edges). The latitude-longitude midpoints of a primal or dual cell are denoted, respectively, by X_i or X_w. See Figure 3 for details. Distances and areas are calculated using the latitude-longitude curves.

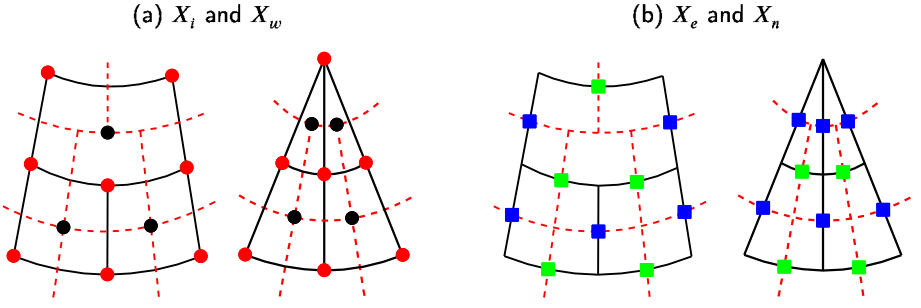

Figure 3: Cells and points given by latitude-longitude midpoints. Black lines are primal edges. Red dashed lines are dual edges. Center points X_i (black) and vertex positions X_w (red) are shown for each primal cell. Zonal wind points X_e (blue) and meridional wind positions X_n (green) are placed at the intersection of primal and dual edges.

Each operator, function, or approximation is defined in one of these sets of points. The index of each object will designate the corresponding set of points.

- We will represent individual primal cells as Ω_i, and primal edges as Γ_e, Γ_n. Dual cells are represented as Ω_w, and dual edges are represented via Γ_e^{dual} and Γ_r^{dual}. The area of a primal or dual cell are respectively given by A_i and A_w. Zonal or meridional metric lengths of primal or dual edges crossing at an X_e point are $\Delta x_e, \Delta y_e$. Metric length of edges intercepting at an X_n point are denoted by $\Delta x_n, \Delta y_n$.
- Prognostic variables are the layer thickness/depth, h_i, placed at cell centers, the staggered zonal wind component, u_e, and meridional wind component, v_n.

- Constants and fixed functions are the gravity acceleration, g, rotation velocity, Ω, sphere radius, a, topography, b_i, and Coriolis function, $f_w = 2\Omega \sin \varphi_w$.

- Auxiliary variables are relative vorticity, ζ_w, absolute vorticity, $\xi_w = \zeta_w + f_w$, potential vorticity, $q_w = \xi_w / h_w^{(q)}$, kinetic energy, K_i, and geopotential, $\Phi_i = g(h_i + b_i)$. Quadrature for hu over Γ_e is denoted by U_e. Quadrature for hv over Γ_n is written as V_n.

- Interpolations will have an upper parenthesis index indicating a variable related to that set of points (h, q, u or v). For instance, $h_e^{(u)}$, $h_n^{(v)}$, and $h_w^{(q)}$ are approximations for thickness at points X_e, X_n, and X_w, respectively.

- Final approximations are the divergence, $[\nabla \cdot h\vec{u}]_i$, the non-linear Coriolis term, $[(\zeta + f)v]_e$, $[(\zeta + f)u]_n$, and gradient components, $[\partial_x(K + \Phi)]_e$, $[\partial_y(K + \Phi)]_n$.

To express the equations related to conservation properties, we will need to employ some extra notation for sets of points.

- The syntax $e \in \mathcal{E}$ indicates all indexes of meridional edge points in the grid. Analogously, for $i \in \mathcal{I}$, $n \in \mathcal{N}$, and $w \in \mathcal{W}$.

- Given a center point index i, the syntax $n \in \mathcal{N}_{\mathcal{I}}^{\text{north}}(i)$ represents the indices of north zonal edges of the cell around X_i. Far from reduction lines, this notation presents only one index. Analogously, for $n \in \mathcal{N}_{\mathcal{I}}^{\text{south}}(i)$, $e \in \mathcal{E}_{\mathcal{I}}^{\text{east}}(i)$, and $e \in \mathcal{E}_{\mathcal{I}}^{\text{west}}(i)$.

2.5. Second-order explicit time-step

While there are different options for time integration (Durran, 2011), here we will adopt an explicit time stepping scheme, avoiding therefore potential restrictions in parallel computing communication existing for many time-implicit schemes.

Wicker and Skamarock (2002) described an explicit Runge-Kutta scheme with three stages and second-order suitable for fluid models. This option has the same region of absolute stability as the third-order Runge-Kutta method. However, the order is smaller and there is no need to keep the intermediate steps in the computer memory.

Let the semi-discrete system of ordinary differential equations be written as $\Psi' = F(\Psi, t)$, with initial condition $\Psi(t_0) = \Psi_0$. Consider a set of time instants $t_k = t_0 + k\Delta t$ and represent Ψ_k as an approximation to $\Psi(t_k)$. Index k is a natural number $k = 0, 1, 2, \ldots, k_{\max}$. We can calculate each time-step of Wicker and Skamarock scheme using two intermediate steps, Ψ^* and Ψ^{**}, following

$$\begin{aligned} \Psi^* &= \Psi_k + F(\Psi_k, t_k)\Delta t/3, && (7)\\ t^* &= t_k + \Delta t/3, \\ \Psi^{**} &= \Psi_k + F(\Psi^*, t^*)\Delta t/2, && (8)\\ t^{**} &= t_k + \Delta t/2, \\ \Psi_{k+1} &= \Psi_k + F(\Psi^{**}, t^{**})\Delta t. && (9) \end{aligned}$$

We will employ a similar scheme. The only difference is the coefficient in the first intermediate calculation. Instead of $\Delta t/3$, we will use $\Delta t/2$. This alteration yields a region of absolute stability that covers a larger section of the imaginary axis (see figure 4). This property allows larger time-steps for oscillatory problems (Durran, 2011), and helps the resulting shallow-water model by preventing short-wavelength errors. The coefficient $\Delta t/2$ maximizes the imaginary-axis interval covered by the region of absolute stability among Runge-Kutta methods with 3 stages and order 2.

3. Discrete properties and filtering on reduced grids

3.1. Motivation for trigonometric approximations

When we increase the resolution of a reduced grid, two different situations occur affecting the consistency of approximations. For a given latitude φ_0 outside the polar first row, the number of cells will increase, providing smaller angular distances ($\Delta\lambda$, $\Delta\varphi$) and improving the results. On the other hand, the number of points around polar points will

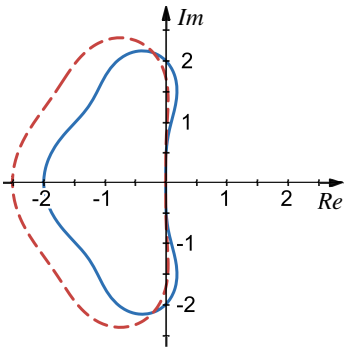

Figure 4: Region of absolute stability for Wicker and Skamarock (dashed red boundary) or the proposed scheme used in this work (continuous blue border). The intersection with the imaginary axis increases from $[-1.73, 1.73]$ to $[-2, 2]$.

remain the same. The approximations have to work adequately in this situation ($\Delta\varphi$ decreases, but $\Delta\lambda$ is the same). We will describe this requirement showing an example.

Consider a plane tangent to the north pole of the sphere. Choose a positive orthonormal basis $\{e_1, e_2\}$ for this plane. Using this basis, we can represent each point of the plane as $X = R\cos(\lambda)e_1 + R\sin(\lambda)e_2$, where R and λ define polar coordinates relative to the basis (see Figure 5), where we have, on purpose, used the longitude λ to represent the angle variable. In this tangent basis, for $R > 0$, the projected direction vectors related to east and north are, respectively, $i = -\sin(\lambda)e_1 + \cos(\lambda)e_2$ and $j = -\cos(\lambda)e_1 - \sin(\lambda)e_2$. If the polar vector wind is a constant, then the components u and v are first-order trigonometric polynomials. For instance, if $\vec{u} = e_2$ then $u = \cos(\lambda)$ and $v = -\sin(\lambda)$. (See Figure 5)

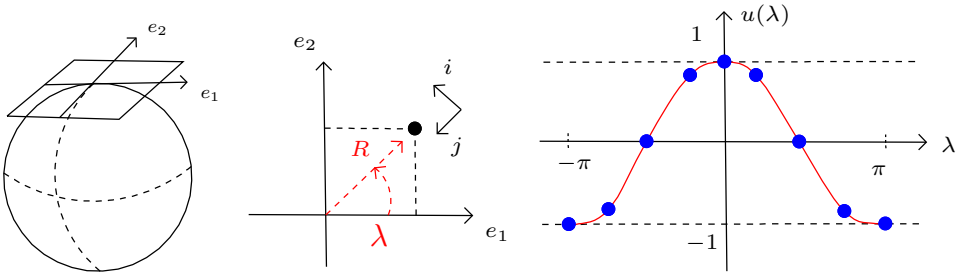

Figure 5: Plane tangent to the north pole (left), coordinates λ and R (center), and representation of zonal wind when $\vec{u} = e_2$ at the polar point (right). Blue points indicate the values considered by a reduced grid with 8 cells in the first row. The profile for $u(\lambda)$ and the number of points in this row remain the same at any refinement. Thus, polynomial zonal interpolations are inconsistent in this situation.

Independently of the refinements used in a reduced grid, the number of cells around the polar point remains the same. Therefore, the error of a polynomial interpolation for the components u and v of a constant polar wind (defined via tangent plane) does not decrease with increasing resolution (thinner rows near the poles). On the other hand, if the interpolation is exact for first-order trigonometric polynomials, then the approximation is exact for this example with constant wind, and first order accurate for smooth non-constant winds. This can be verified with application of the Taylor theorem on the tangent plane to describe the resulting truncation error. Using second-order trigonometric functions, the approximation is exact for first-order polynomial (tangent) polar wind, and the truncation error has order two for smooth fields.

Purser, Bénard, and Glinton described the consistency of approximations with trigonometric functions in reduced grids using Taylor theorem and change of variables (Purser, 1988) or properties of spherical harmonics (Bénard and Glinton, 2019).

In order to present this motivation, we have considered a specific projection to a tangent plane and employed results from the Taylor theorem on the plane. Therefore, this is not a rigorous demonstration of consistency on the sphere. In the next topics, we will define zonal approximations using trigonometric functions and check their consistency on reduced grids numerically, employing some examples on the sphere. Each approximation will be tested individually (calculating the numerical expression and comparing it with the respective reference value).

3.2. Interpolations, derivatives, and quadratures

We will consider polynomial and trigonometric approximations obtained by a similar process. First, we write a linear combination of the variable using the points where it is known. Then, we calculate the coefficients to achieve the exact value when the function is in a specific subspace.

Some expressions will have an extra requirement of symmetry. Using transitions with factor 2, we will need interpolations to midpoints and quarter-points. The coefficients will be symmetric when the intervals also have this property. Bénard and Glinton (2019) describe approximations to any intermediate position, but, even for a midpoint, those expressions are not symmetrical.

Each notation will indicate a different approximation: I for interpolation, Q for line quadrature, or D for discrete derivative, on sphere, in each direction (with subindex x for zonal, or y for meridional). Functions will be indicated with respect to specific subspaces: P for polynomials or T for trigonometric. Appendix A shows the full expression of each approximation and the corresponding set of functions exactly represented.

Following, we will present the expression of two operators for zonal interpolation, describe one consistency test in the sphere, and indicate the order observed in a set of numerical tests.

3.2.1. Example with zonal interpolation

Consider a function $f(\lambda)$ and a set of zonal points with uniform angular space $\Delta\lambda$. We will describe two symmetric options for interpolation in the midpoint.

1. With polynomials and 4 values, the linear combination is

$$I_{xP4}[f](\lambda) = a_1 f(\lambda - 1.5\Delta\lambda) + a_0 f(\lambda - 0.5\Delta\lambda) + a_0 f(\lambda + 0.5\Delta\lambda) + a_1 f(\lambda + 1.5\Delta\lambda). \tag{10}$$

   The coefficients a_0 and a_1 are chosen to make this approximation exact when $f(\lambda) = 1$, $f(\lambda) = \lambda$, $f(\lambda) = \lambda^2$, or $f(\lambda) = \lambda^3$.
2. Using trigonometric functions and 4 points, the expression is

$$I_{xT4}[f](\lambda) = a_1 f(\lambda - 1.5\Delta\lambda) + a_0 f(\lambda - 0.5\Delta\lambda) + a_0 f(\lambda + 0.5\Delta\lambda) + a_1 f(\lambda + 1.5\Delta\lambda). \tag{11}$$

   Coefficients a_0 and a_1 are calculated to make the result exact when $f(\lambda) = 1$, $f(\lambda) = \sin(\lambda)$, or $f(\lambda) = \cos(\lambda)$. These coefficients are different for each value of $\Delta\lambda$, therefore, may vary for distinct latitude circles.

Some examples lead to computational tests with higher consistency order than usual. For instance, situations without polar wind or configurations given by trigonometric polynomials on each latitude line. We will consider a wind field without these characteristics and show the error of two interpolation alternatives using reduced grids (see figure 6). The first graphic of errors employs the polynomial interpolation with 4 values for midpoints, and the second uses the trigonometric. The horizontal axis is latitude. The vertical axis is the relative error with logarithmic scale. Each gray rectangle indicates a factor of 4. Each curve shows the error on the same longitude column, but with a different resolution for the reduced grid. When the approximation has order 2, the consecutive curves have 1 gray rectangle of distance. Far from polar points, both options have order 4. In the polar region, the polynomial has order zero and the trigonometric has order 1. Tests using other longitudes and other wind fields provided similar estimates of order.

Consistency/truncation order depends on the region, if it includes or not the polar region, and the type of function (scalar field or component of a vector field). As used in Sadourny (1975) and Arakawa and Lamb (1981), on a regular latitude-longitude grid, I_{xP2} would have second order in the polar region, primarily due to the concentration of points at the poles. However, on reduced grids, this is not the case. Table 1 shows the order of some options for zonal interpolation. Columns indicate the order in each region and for each type of function (u, v for wind components or h for scalar function). To get order 2 in the polar region, we can use trigonometric functions and 6 points.

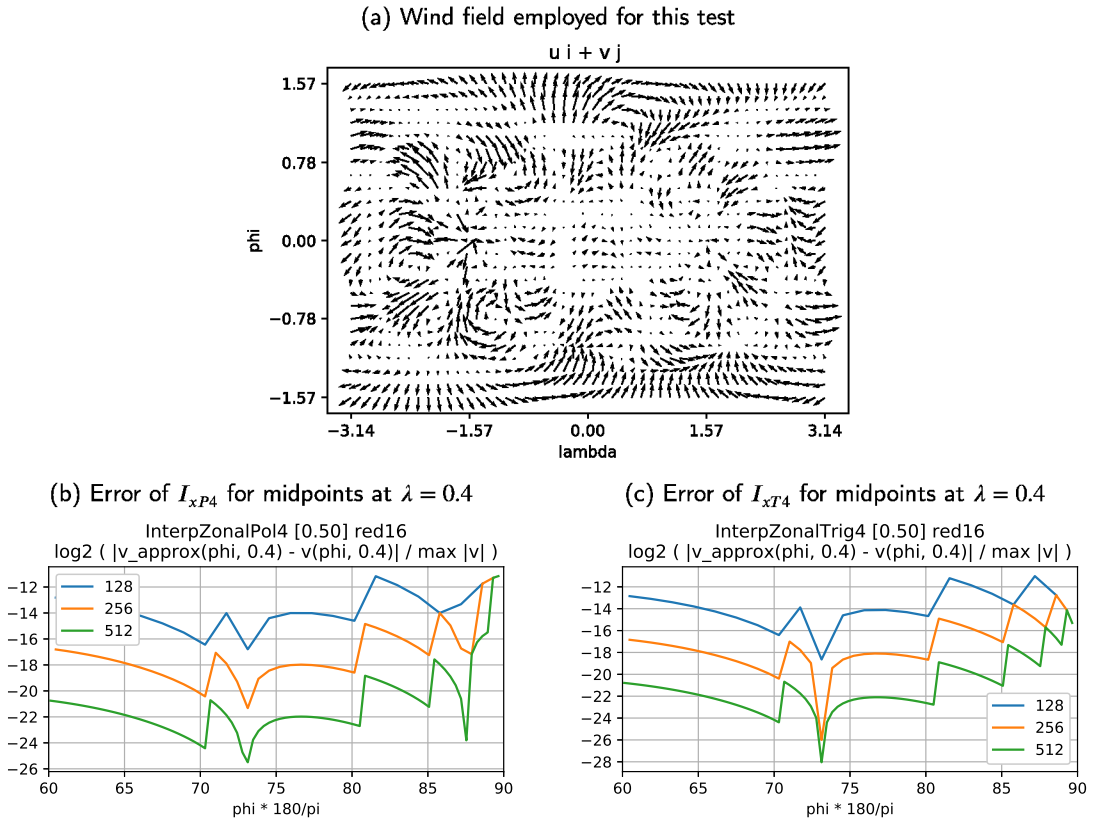

Figure 6: Example with polar wind (a), error with polynomial interpolation (b), and error with trigonometric approximation (c). Each curve shows the relative error on a longitude column using a different grid resolution. In regions where the approximation has order 2, the distance between consecutive curves is 1 gray rectangle. Polynomial interpolation is not consistent in polar regions of a reduced grid.

Approximation	Polar region		Outside polar region	
	u, v	h	u, v	h
I_{xP2}	0	1	2	2
I_{xP4}	0	1	4	4
I_{xT4}	1	2	4	4
I_{xT6}	2	3	6	6

Table 1
Consistency/truncation order of some zonal interpolations on a reduced grid. Polynomial interpolations are not consistent for situations wind in polar region. Using trigonometric interpolations and more points, the consistency order increases.

3.3. Discrete Gauss-Stokes expression with C-staggered reduced grids

Finite difference approximations for divergence can provide schemes with high consistency order (Bénard and Glinton, 2019). Finite volumes expressions can lead to methods with mass conservation (Sadourny, 1975; Ringler et al., 2010). We will describe a discrete approximation related to the Gauss-Stokes theorem and test some options for line quadratures and the reference point.

Consider a vector field, $\vec{u} = ui + vj$, a latitude-longitude rectangle, Ω, and boundaries at each cardinal direction, $\Gamma^E, \Gamma^W, \Gamma^N, \Gamma^S$. If the vector field is smooth, then Gauss-Stokes theorem provides an alternative option to calculate

Approximation	Polar region	Outside polar region
$G^{(\mathrm{mid})}_{xP1,yP1}$	−1	2
$G^{(\mathrm{mid})}_{xT5,yP1}$	1	2
$G^{(\mathrm{mid})}_{xT7,yP3}$	1	2
$G^{(\mathrm{cm})}_{xT5,yP1}$	1	2
$G^{(\mathrm{cm})}_{xT7,yP3}$	2	2

Table 2
Consistency orders of some discrete divergence based on Gauss-Stokes approximations on a reduced grid. Option with polynomial quadratures and one point is not consistent. Using zonal trigonometric quadrature and projected center of mass, we obtain a second-order approximation

the integral of divergence

$$\int_\Omega \nabla\cdot\vec{u} = \int_{\Gamma^N} v - \int_{\Gamma^S} v + \int_{\Gamma^E} u - \int_{\Gamma^W} u. \tag{12}$$

We will apply a quadrature to each of these integrals. The surface quadrature will be the divergence in one point $(\lambda_0,\varphi_0)\in\Omega$ multiplied by the latitude-longitude rectangle area $|\Omega|$. This approximation has error $E_{\mathrm{surf}}(\Omega,\vec{u},\lambda_0,\varphi_0)$. Zonal and meridional line quadratures $Q_x[\Gamma,v]$ and $Q_y[\Gamma,u]$ are approximations with error $E_{Q,x}(\Gamma,v)$ and $E_{Q,y}(\Gamma,u)$. The relation between integrals, quadratures, and errors are

$$\int_\Omega \nabla\cdot\vec{u} = (\nabla\cdot\vec{u})(\lambda_0,\varphi_0)|\Omega| + E_{\mathrm{surf}}(\Omega,\vec{u},\lambda_0,\varphi_0), \tag{13}$$

$$\int_{\Gamma^N} v = Q_x(\Gamma^N,v) + E_{Q,x}(\Gamma^N,v), \tag{14}$$

$$\int_{\Gamma^E} u = Q_y(\Gamma^E,u) + E_{Q,y}(\Gamma^E,u). \tag{15}$$

As a result, we obtain an approximation to the divergence at a given point as $G[\Omega,\vec{u}](\lambda_0,\varphi_0)$, and an error, $E_G[\Omega,\vec{u}](\lambda_0,\varphi_0)$, that depends on each quadrature error. The relation between divergence, discrete Gauss expression, and error can be summarized as

$$(\nabla\cdot\vec{u})(\lambda_0,\varphi_0) = G[\Omega,\vec{u}](\lambda_0,\varphi_0) + E_G[\Omega,\vec{u}](\lambda_0,\varphi_0), \tag{16}$$

where the approximations and errors are given by (omitting the point of interest for brevity)

$$G[\Omega,\vec{u}] = \frac{1}{|\Omega|}\left(Q_x(\Gamma^N,v) - Q_x(\Gamma^S,v) + Q_y(\Gamma^E,u) - Q_y(\Gamma^W,u)\right), \tag{17}$$

$$E_G[\Omega,\vec{u}] = \frac{1}{|\Omega|}\left(E_{Q,x}(\Gamma^N,v) - E_{Q,x}(\Gamma^S,v) + E_{Q,y}(\Gamma^E,u) - E_{Q,y}(\Gamma^W,u) - E_{\mathrm{surf}}(\Omega,\vec{u})\right). \tag{18}$$

Consistency order for this discrete expression depends on the region on the sphere and the options for each quadrature. For line integrals, we can choose among polynomial or trigonometric quadratures and select the number of points. For surface integral, we can decide the position of the reference point. Du et al. (2003) described the use of projected centers of mass for Voronoi grids in a surface. Sadourny, Arakawa, and Lamb considered rectangular midpoints for latitude-longitude grids (Sadourny (1975); Arakawa and Lamb (1981)). We will test these two options for reduced grids with latitude-longitude rectangular cells.

The notation will indicate the reference point (*mid* for latitude-longitude midpoint or *cm* for the projected center of mass) and the options for quadratures in each direction. For instance, $G^{(\mathrm{mid})}_{xT3,yP1}$ uses midpoints, zonal trigonometric quadrature with 3 points, and meridional polynomial quadrature with 1 point.

Table 2 shows the consistency orders of some options for this expression. To obtain order 2, we can use the centroid, trigonometric zonal quadratures, and polynomial meridional approximations.

Approximation	Polar region		Outside polar region	
	u, v	h	u, v	h
F_{xS3}	0	1	2	2
F_{xS5}	0	1	4	4
F_{xT5}	1	2	4	4
F_{xT7}	2	3	6	6

Table 3
Consistency/truncation order of some zonal local filters on a reduced grid. Shapiro's zonal filters are not consistent for situations with polar wind. Using trigonometric filters and more points, the consistency order increases.

For a latitude-longitude grid, $G^{(\mathrm{mid})}_{xP1,yP1}$ would have truncation error of order one in the polar region. Sadourny, Arakawa, and Lamb employed this approximation (Sadourny (1975); Arakawa and Lamb (1981)). The approximation $G^{(\mathrm{cm})}_{xT7,yP3}$ has order 2 on reduced grids, but it uses more calculations. The option $G^{(\mathrm{mid})}_{xT5,yP1}$ has first-order, but it is less expensive.

We can apply a similar expression to approximate relative vorticity $\zeta = k \cdot \nabla \times \vec{u}$. With a C-staggered grid, the positions are convenient to calculate divergence near the center of primal cells and vorticity near the vertices.

3.4. Interpolation with damping for short waves

To prevent non-linear instability, we can employ a method with several conservation properties (Arakawa, 1966; Sadourny, 1975; Arakawa and Lamb, 1981) or limit the use of short waves (Shapiro, 1975; Jablonowski and Williamson, 2011).

Shapiro (1975) described a set of one-dimensional local filters that preserve the constant function and remove the shortest wave. Using a larger stencil, the damping of long waves decreases. Bénard and Glinton (2019) used two distinct filters. In polar regions, the method employs a complete Fourier filter. Far from polar points, they apply an expression related to a linear combination of Shapiro's filters.

We will use trigonometric functions to obtain a local zonal filter exact for the longest waves, and define a bi-dimensional filter with variable damping (option to control how strong the filter will be). In the section about numerical tests, we will include simulations without filters and others with a weak uniform grid (same expression everywhere).

3.4.1. Filters with one dimension

Consider a function $f(\lambda)$ and a zonal row of points with uniform angular distance $\Delta\lambda = 2\pi/N$. The number of points N is even. Zonal filter with trigonometric functions and 5 points is given by

$$F_{xT5}[f](\lambda) = a_2 f(\lambda - 2\Delta\lambda) + a_1 f(\lambda - \Delta\lambda) + a_0 f(\lambda) + a_1 f(\lambda + \Delta\lambda) + a_2 f(\lambda + 2\Delta\lambda). \tag{19}$$

We calculate the coefficients a_0, a_1 and a_2 to obtain $f(\lambda)$ when $f = 1$ or $f = \sin\lambda$ or $f = \cos\lambda$ and to achieve the value 0 when $f = \cos(N\lambda/2)$.

To control the damping, we will take a linear combination with the identity operator. Trigonometric zonal filter with 5 points and damping $\mu \in [0, 1]$ is written as

$$F^{\mu}_{xT5}[f](\lambda) = (1 - \mu) f(\lambda) + \mu F_{xT5}[f](\lambda). \tag{20}$$

For instance, if $\mu = 0.1$, then the shortest wave is multiplied by 0.9.

Notation for one-dimensional filters will indicate the damping factor μ, direction (x for zonal or y for meridional), option that defines the coefficients (T for trigonometric or S for Shapiro), and the number of points. To apply a meridional filter in a reduced grid, we need to use zonal interpolations.

Trigonometric and Shapiro's filters have the same consistency in a reduced grid as the corresponding trigonometric and polynomial interpolation (See table 3). The choice of damping coefficient $\mu \in [0, 1]$ does not affect the order. Shapiro's filters have consistency zero for wind components in polar regions. The trigonometric filter with 7 points has second-order. Using a full latitude-longitudeg grid, Shapiro's filter with 3 points would have order 2 near the polar points.

3.4.2. Filters with two dimensions

The two-dimensional filters will be a composition. Notation will present the options for each direction. Zonal interpolation uses trigonometric functions and one point less than the zonal filter. For instance, this is the definition of a filter using F^{μ}_{xT5} and F^{μ}_{yS3},

$$F^{\mu}_{xT5,yS3}[f](\lambda,\varphi) = (F^{\mu}_{yS3} \circ I_{xT4} \circ F^{\mu}_{xT5}[f])(\lambda,\varphi). \tag{21}$$

We apply the zonal filter, then the zonal interpolation (if necessary), and then the meridional filter.

3.5. Conservation of mass in a reduced grid

Our motivation to approximate the divergence with a finite volumes expression is the interest in mass conservation. We will consider the approximation described in the previous topics and verify this conservative property.

Consider primal cells, Ω_i, line quadratures for hu at meridional edges, U_e, and line quadratures for hv at zonal edges, V_n. Volume is a discrete integral using the thickness and area of each primal cell. We can write this definition as

$$\mathbb{V} = \sum_{i\in\mathcal{I}} h_i A_i. \tag{22}$$

Calculating a derivative in time and applying the semi-discrete mass equation, we obtain

$$\partial_t \mathbb{V} = \sum_{i\in\mathcal{I}} \partial_t h_i A_i = -\sum_{i\in\mathcal{I}} [\nabla\cdot h\vec{u}]_i A_i. \tag{23}$$

If the divergence is approximated by one of the discrete Gauss-Stokes expressions from the previous topics, then we can write

$$\partial_t \mathbb{V} = -\sum_{i\in\mathcal{I}} \left(+ \sum_{e\in\mathcal{E}^{\text{east}}_{\mathcal{I}}(i)} U_e - \sum_{e\in\mathcal{E}^{\text{west}}_{\mathcal{I}}(i)} U_e + \sum_{n\in\mathcal{N}^{\text{north}}_{\mathcal{I}}(i)} V_n - \sum_{n\in\mathcal{N}^{\text{south}}_{\mathcal{I}}(i)} V_n \right). \tag{24}$$

Each line quadrature, U_e, V_n, is used by two consecutive cells. One cell applies a positive sign and the other uses a negative sign. The complete summation becomes zero, showing that the volume does not change.

Analogously, we can show that discrete Gauss-Stokes expressions for relative vorticity provide a discrete integral equal to zero,

$$\sum_{w\in\mathcal{W}} \zeta_w A_w = 0. \tag{25}$$

These results remain true for any expression used for line quadratures.

4. A method with trigonometric functions

Purser (1988) described the use of trigonometric functions to obtain interpolations and discrete derivatives consistent on reduced grids. Bénard and Glinton (2019) proposed a method for shallow-water equations employing these approximations. Their scheme has trigonometric finite-differences, non-staggered reduced grids, smooth variation in the number of cells of each row, and high order of consistency (for large stencils). This method does not have conservation properties, a complete Fourier filter is used at polar regions, and simulations indicate weak short-wavelength errors.

We will study a scheme employing trigonometric finite differences, finite volumes, C-staggered grid, transitions with factor 2, order one or two of consistency, conservation of mass, and stencils with at most 7 points in zonal direction and 3 in meridional direction.

The use of trigonometric approximations will result in consistency at polar regions. C-staggered grid avoids the stationary gravity waves and helps the use of finite volumes. Gauss approximation for divergence will cause conservation of mass. Transitions with factor 2 permit the use of symmetrical coefficients for most approximations

(it prevents short wave-length errors). Stencils of 7 by 3 permit the communication of 3 columns or 1 row across the boundary of each processing region (it helps the efficiency with parallel programming).

Some tests showed good behavior even without any filtering. Others required a small dissipation. The space filter has the same consistency order as the other interpolations employed in this method (even in polar regions). The sequence of calculations for kinetic energy and Coriolis objects is different from the options used by Sadourny, Arakawa, Lamb, Ringler, and others (Sadourny, 1975; Arakawa and Lamb, 1981; Ringler et al., 2010). For instance, kinetic energy will have two interpolations and then two products. The change in these approximations improved the stability in the numerical tests.

4.1. Approximations

We will describe the approximations in a region without transitions. Consider the notations presented at section 2.4. Near the reductions, zonal interpolation I_{xT6} is applied if necessary. Around polar points some small adequations are needed. For instance, meridional interpolation for v in the first row will include points from a geodesic line crossing the polar point.

Averages of thickness are trigonometric or polynomial second-order interpolations. Divergence and vorticity are Gauss discrete approximations with order one. They can be written as

$$h_e^{(u)} = I_{xT6}[h_i], \tag{26}$$
$$h_n^{(v)} = I_{yP2}[h_i], \tag{27}$$
$$h_w^{(q)} = I_{yP2} \circ I_{xT6}[h_i], \tag{28}$$
$$[\nabla \cdot h\vec{u}]_i = G^{(\mathrm{mid})}_{xT5,yP1}[h_e^{(u)}u_e, h_n^{(v)}v_n], \tag{29}$$
$$\zeta_w = G^{(\mathrm{mid})}_{xT5,yP1}[v_n, -u_e], \tag{30}$$
$$\xi_w = \zeta_w + f_w. \tag{31}$$

Averages of wind components are second-order interpolations. Kinetic energy is a product of interpolations and does not use areas as a weight (this option is different from the polynomial method). Derivatives are second-order approximations. Their expressions are

$$u_i^{(h)} = I_{xT6}[u_e], \tag{32}$$
$$v_i^{(h)} = I_{yP2}[v_n], \tag{33}$$
$$K_i = (u_i^{(h)}u_i^{(h)} + v_i^{(h)}v_i^{(h)})/2, \tag{34}$$
$$\Phi_i = g(h_i + b_i), \tag{35}$$
$$[\partial_x(K+\Phi)]_e = D_{xT4}[K_i + \Phi_i], \tag{36}$$
$$[\partial_y(K+\Phi)]_n = D_{yP2}[K_i + \Phi_i]. \tag{37}$$

Average of wind and vorticity are second-order composite interpolations. Coriolis objects are products of interpolations and do not use h as a weight (they are different from the polynomial method). We can represent then as

$$u_n^{(v)} = I_{yP2} \circ I_{xT6}[u_e], \tag{38}$$
$$v_e^{(u)} = I_{yP2} \circ I_{xT6}[v_n], \tag{39}$$
$$\xi_e^{(u)} = I_{yP2}[\xi_w], \tag{40}$$
$$\xi_n^{(v)} = I_{xT6}[\xi_w], \tag{41}$$
$$[\xi v]_e = \xi_e^{(u)}v_e^{(u)}, \tag{42}$$
$$[\xi u]_n = \xi_n^{(v)}u_n^{(v)}. \tag{43}$$

If a nonzero damping coefficient μ is given, then a second-order two-dimensional filter is applied for u_e, v_n, and h_i at the end of each time step. We can implement Shapiro's filter with 5 points as a composition of two transformations with 3 points. The spacial filters are

$$h_i^{\mathrm{new}} = F^{\mu}_{xT7,yS5}[h_i], \tag{44}$$

$$u_e^{\text{new}} = F^{\mu}_{xT7,yS5}[u_e], \tag{45}$$

$$v_n^{\text{new}} = F^{\mu}_{xT7,yS5}[v_n]. \tag{46}$$

All approximations have order one or two of consistency everywhere in the reduced grid. Far from polar regions, the order is bigger. This method has mass conservation. Numerical tests with one week showed results similar to Sadourny's method (latitude-longitude grid, conservation of mass and total energy).

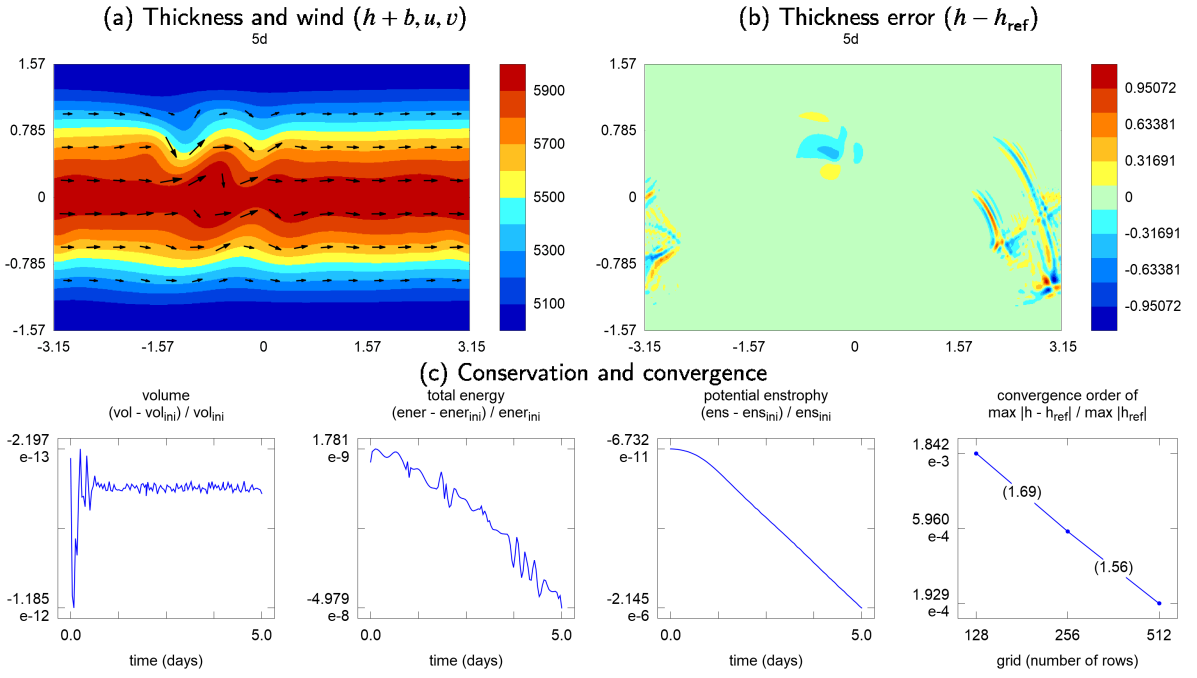

Figure 7: Results using the trigonometric method and the example with zonal wind and a smooth mountain. Errors do not have an accumulation at reductions. Total energy and potential enstrophy decrease. The order of convergence was near 1.7.

4.2. Numerical tests for convergence and accumulation of error

Tests with a few days and resolution of $40Km$ were stable even without any filtering ($\mu = 0$). We applied the following examples: zonal wind with a Gaussian mountain, Haurwitz wave with number 4, zonal wind with instability, and zonal wind with grid rotated by 45 degrees (Williamson et al., 1992; Galewsky et al., 2004). Figures 7, 8, and 9 present the results obtained for some examples. Grids have a maximum distance of $40Km$. We calculated the errors in thickness using a high-resolution simulation with Sadourny's method (latitude-longitude, conservation of mass and total energy). Figures for scalar functions on the sphere employ latitude-longitude coordinates. Graphics for volume, total energy, and potential enstrophy use a linear scale on the vertical axis. Figures for convergence order employ a logarithmic scale. There is no accumulation of errors in transition lines or polar regions. Errors are similar to Sadourny's method with a maximum edge length of $40Km$. Total energy and potential enstrophy usually decrease. The estimate for convergence order assumed a value near 2.

4.3. Numerical tests for stability

Long simulations with steady examples indicated the effects of non-linear instability. Applying the filter with a weak damping factor, the results became stable. We employed three tests: polar wind with large thickness (test case 2 from Williamson et al. (1992) with $\alpha = \pi/4$), polar wind with topography and small thickness (adapted from Peixoto et al. (2018)), and Gaussian pulse with f constant and low resolution (adapted from Peixoto (2016)).

The first example has polar wind and large thickness. Topography is zero. Thickness varies from 1Km to 3Km. The exact field is similar to the first item from figure 9. Figure 10 shows the results with this test. The horizontal axis is time,

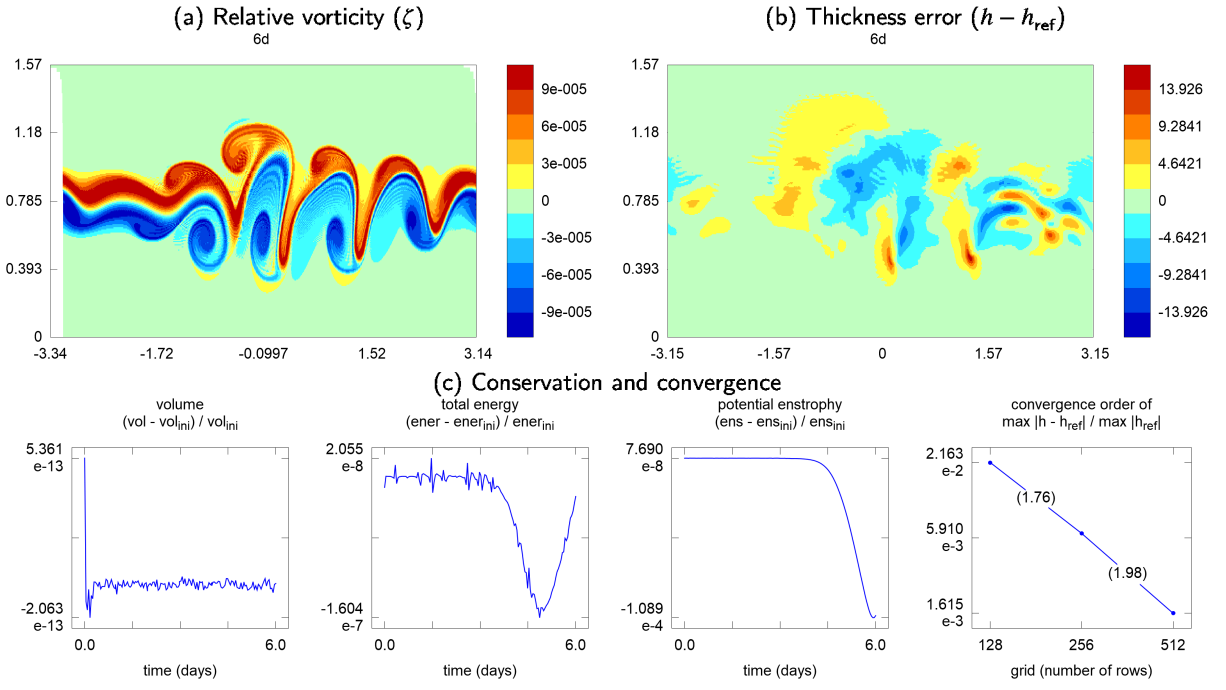

Figure 8: Results using the trigonometric method and the example with zonal wind and instability. Errors do not have an accumulation at transitions. The scheme showed an order of convergence near to 1.9.

the vertical axis is a logarithm of the thickness error, and each curve indicates the error with a different grid resolution. When the method has order 2 of convergence, the consecutive curves are one rectangle far from each other. Without filtering, the instability can be seen at day 20 for the grid with 256 rows or at day 10 for 512 rows. With the filter and $\mu = 0.1$, the simulation is stable. The filter did not affect the convergence order. As a comparison, we can observe that this example is stable with Sadourny's method (latitude-longitude grid, mass and total energy conservation, without any filter).

The second test has polar wind, topography, and a small thickness. This is a particular choice for the examples described by Peixoto et al. (2018). Topography varies from 0m to 2Km. Thickness is 1m everywhere. Coriolis function is the usual ($f = 2\Omega \sin\varphi, \Omega = 2\pi/86400$). The field for $h+b$ is similar to the first item in figure 9, but with values from 1m to 2001m. This test can indicate the presence of some different instability processes, including the one described by Hollingsworth et al. (Hollingsworth et al., 1983; Peixoto et al., 2018). Figure 11 presents the results using this test. Without damping, the instability begins in the first hours of simulation. With the filter and damping $\mu = 0.1$, the results were stable and the convergence order was close to 2. Sadourny's method is unstable for this example (without damping).

The third situation is a Gaussian small pulse with low resolution and f constant. This example was adapted from a test used by Peixoto (2016). We changed the equations from a trigonometric function to a Gaussian. This alteration gave us more freedom to adjust the conditions. The parameters are the sphere radius $a = 6.371{\times}10^6$, gravity $g = 9.806$, sphere rotation velocity $\Omega = 7.292 \times 10^{-5}$, basic thickness $H_0 = 6001$, pulse amplitude $h_0 = 50$, pulse radius factor $R_0 = 0.15$, null topography $b = 0$, and the central coordinates $\lambda_0 = 0.786$ and $\varphi_0 = 0.784$. The constant Coriolis function f_0 and the initial conditions $h_{\text{ini}}, u_{\text{ini}}, v_{\text{ini}}$ can be written as

$$S(\lambda,\varphi) = (\cos\varphi\cos\lambda - \cos\varphi_0\cos\lambda_0)^2 + (\cos\varphi\sin\lambda - \cos\varphi_0\sin\lambda_0)^2 + (\sin\varphi - \sin\varphi_0)^2, \quad (47)$$

$$h_{\text{ini}}(\lambda,\varphi) = H_0 + h_0 \exp\left(\frac{-S(\lambda,\varphi)}{(R_0)^2}\right), \quad (48)$$

$$f_0 = 2\Omega\sin(\varphi_0), \quad (49)$$

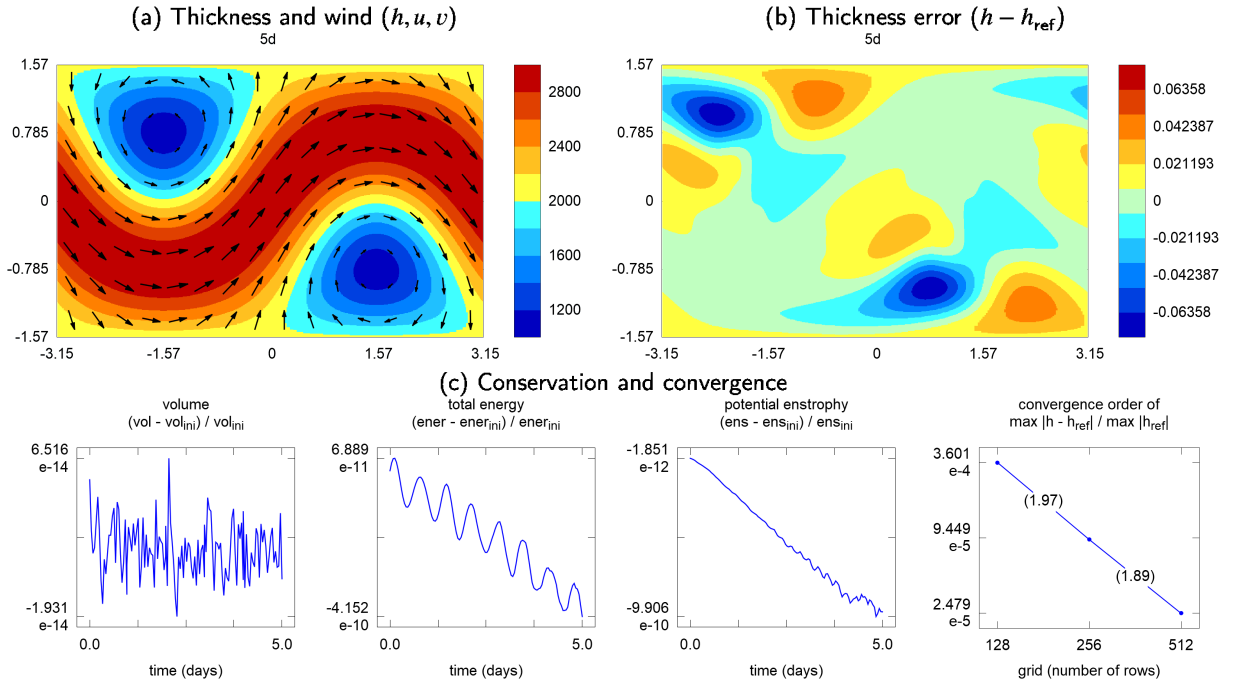

Figure 9: Results using the trigonometric method and the example with polar wind and large thickness. Errors do not have an accumulation in polar regions. Total energy and potential enstrophy decrease. The order of convergence was near to 2.

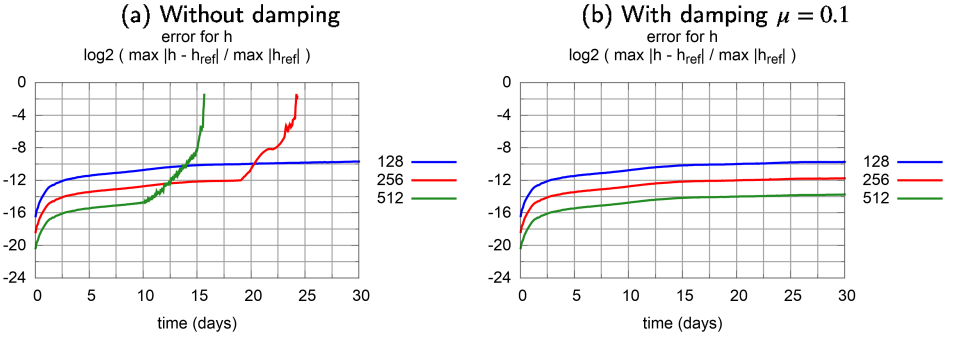

Figure 10: Results from trigonometric method with the example with polar wind and large thickness (test case 2 rotated by 45 degrees). Without damping, the numerical instability begins after 10 or 20 days. With a small damping factor, the simulation became stable and indicated second order of convergence.

$$u_{\text{ini}}(\lambda, \varphi) = \frac{-g}{f_0} \frac{1}{a} \frac{\partial h_{\text{ini}}}{\partial \varphi}(\lambda, \varphi), \tag{50}$$

$$v_{\text{ini}}(\lambda, \varphi) = \frac{g}{f_0} \frac{1}{a \cos(\varphi)} \frac{\partial h_{\text{ini}}}{\partial \lambda}(\lambda, \varphi). \tag{51}$$

Figure 12 shows the graphics obtained using this test and a reduced grid with 64 rows. The pulse is represented by 10 rows and less than 16 columns. There is a reduction line crossing the pulse. Without filtering, the initial field is almost preserved until day 30. With a filter coefficient $\mu = 0.1$, the pulse amplitude decreased by a half after 30 days.

We must consider two effects to decide the damping factor in a long simulation. If the filter is too weak, it may be unable to prevent instability. If the filter is too strong, we may lose a lot of information.

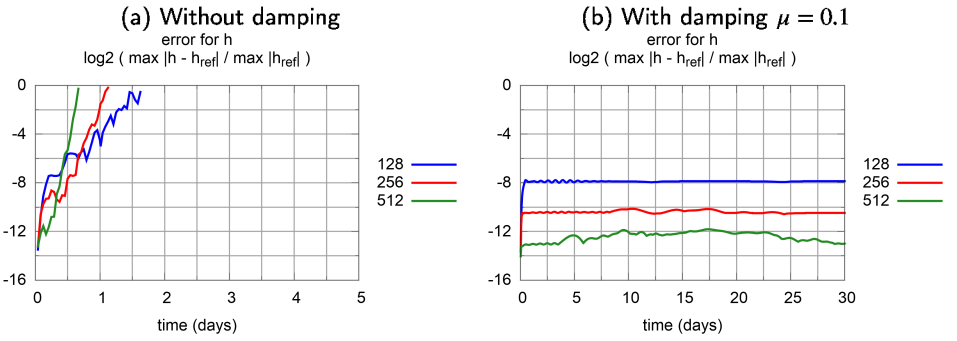

Figure 11: Results using the trigonometric method and the example with polar wind, sphere with rotation, topography from 0 to 2Km, and 1m thickness. Without damping, the instability begins before 12h. With a damping factor $\mu = 0.1$, the simulation was stable and indicated an order of convergence near to 2. This is a very challenging test for stability.

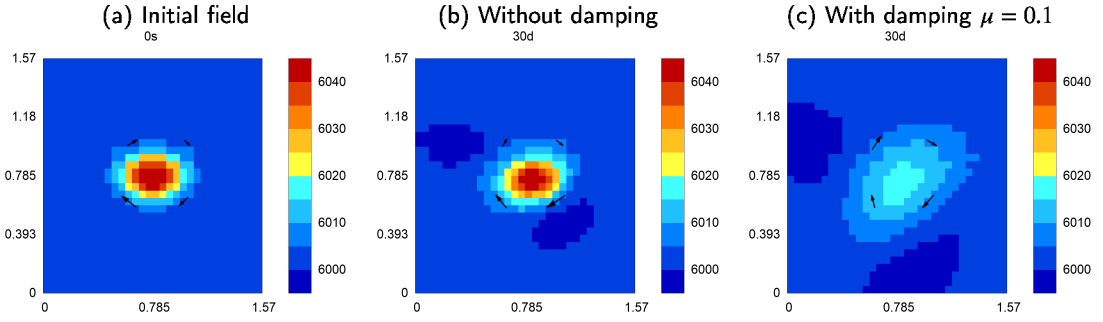

Figure 12: Results using the trigonometric method and a Gaussian small pulse with low grid resolution and a f-sphere (f =constant). Without damping, the original signal is almost preserved. With a damping factor $\mu = 0.1$, the pulse is still present after 30 days, but its amplitude decreased by half. There is a transition line near to 45 degrees.

4.4. Computational cost and other implementations

Table 4 indicates the processing time of Sadourny or trigonometric method using one 3GHz core. We chose the same number of rows and simulated test case 2 with rotation of 45° for one day. Each column shows the measures for one method. The trigonometric scheme reaches a smaller error using fewer cells and a larger time-step. The increase in time per cell occurred with a factor near 2. By repeating the tests, the total processing time varied less than 3% related to the values in this table.

The trigonometric method employs approximations with more points than Sadourny's method or TRSK. The mean computational cost at each time step for one cell increased. With distributed memory, the communication cost would also be larger. TRSK shares only the cells touching each processing region boundary. Trigonometric method shares 3 columns or 1 row at each border. This requirement has a cost comparable to other implementations in the 3-dimensional model. Higher-order schemes for advection of tracers demand the communication of 2 cells at each boundary.

In the topic about discrete Gauss-Stokes approximations on reduced grids, we described one alternative with second order of consistency. To employ this option, the method has to calculate some objects on projected centers of mass and others on latitude-longitude midpoints. We can attend to this requirement by using some extra meridional interpolations. It allows us to obtain a method where all approximations have order 2 or 3 of consistency. Implementation becomes somewhat more complicated. The amount of information exchanged in region boundaries increases (2 rows or 4 columns). The error becomes smaller in the simulations. Instability begins later. However, the behavior is almost the same. This method also achieves a convergence order near to 2 and needs a weak filter on long simulations.

	Sadourny (latitude-longitude grid)	Trigonometric without damping	Trigonometric with damping $\mu = 0.1$
Number of cells in the grid with 128 rows	32768	22752	22752
Time-step (0.9 of CFL value)	10 s	193 s	193 s
Relative thickness error ($\max \lvert h - h_{\text{ref}} \rvert$ / $\max \lvert h_{\text{ref}} \rvert$)	2.77E-04	9.91E-05	9.77E-05
Total processing time	65.84 s	4.54 s	5.07 s
Mean time for one time-step at each cell	2.33E-07 s	4.46E-07 s	4.98E-07 s

Table 4
Comparison using simulations of 1 day with the test case 2 and rotation of 45° (Williamson et al., 1992). Columns indicate each method and rows describe some measures. The trigonometric method uses fewer cells, has a larger time-step, and achieves a smaller error. The time per cell increased with a factor near 2.

5. Concluding remarks

We studied some alternatives for approximations with global reduced grids adapting results from TRSK and the method of Bénard and Glinton. These approximations can be combined to describe a method. Depending on the alternatives employed, the resulting scheme shows different properties of consistency, conservation and stability. We combined some options to present a method with interesting properties and tested the resulting scheme with numerical simulations.

The proposed method uses symmetrical approximations, is consistent everywhere, has a consistent local filter, and preserves mass. Numerical tests for one week did not need any filter. Results did not show short-scale errors or accumulation in regions of the grid. Convergence rate was near 2. Some simulations with 30 days required a weak filter. Without damping, this scheme was less stable than Sadourny. With a weak filter, the stability was stronger than Sadourny. The capacity of preserving steady processes with low-resolution was similar to TRSK. The average processing time for one time-step in each cell is bigger than with Sadourny or TRSK. Using distributed memory, one row or three columns are shared at each region boundary.

Simulations indicated that the trigonometric method is a good candidate for global models. We intend to study the following topics in a future project. Adapt the scheme to describe reduced grids with local refinement in a rectangular area (transitions in zonal or meridional direction). Employ different approximations at each region to obtain the same consistency order everywhere (smaller computational cost in low and mid-latitudes). Extend the method to represent a global three-dimensional model for atmospheric dynamics.

CRediT authorship contribution statement

Genilson S. Lima: Conceptualization, Methodology, Software, Investigation, Writing - Original Draft. **Pedro S. Peixoto:** Supervision, Methodology, Writing - Review & Editing.

Declaration of competing interest

The authors declare that they have no known competing financial interests or personal relationships that could have appeared to influence the work reported in this paper.

Acknowledgements

We would like to give a special mention to the contribution from Professor Saulo R. M. Barros. He was advisor on the Ph.D. research project that led to this paper. His participation occurred until July 2021, when he passed away.

(a) Interpolations when λ_0 is a midpoint

Interpolation	Expression	Functions such that $I_x[f](\lambda_0) = f(\lambda_0)$
$I_{xP2}[f]$	$a_0 f_{-0.5} + a_0 f_{0.5}$	$1, \lambda$
$I_{xP4}[f]$	$a_1 f_{-1.5} + a_0 f_{-0.5} + a_0 f_{0.5} + a_1 f_{1.5}$	$1, \lambda, \lambda^2, \lambda^3$
$I_{xT4}[f]$	$a_1 f_{-1.5} + a_0 f_{-0.5} + a_0 f_{0.5} + a_1 f_{1.5}$	$1, \sin(\lambda), \cos(\lambda)$
$I_{xT6}[f]$	$a_2 f_{-2.5} + a_1 f_{-1.5} + a_0 f_{-0.5} + a_0 f_{0.5} + a_1 f_{1.5} + a_2 f_{2.5}$	$1, \sin(\lambda), \cos(\lambda), \sin(2\lambda), \cos(2\lambda)$

(b) Interpolations when λ_0 is a quarter-point

Interpolation	Expression	Functions such that $I_x[f](\lambda_0) = f(\lambda_0)$
$I_{xP2}[f]$	$a_0 f_{-0.25} + a_1 f_{0.75}$	$1, \lambda$
$I_{xP4}[f]$	$a_0 f_{-1.25} + a_1 f_{-0.25} + a_2 f_{0.75}$	$1, \lambda, \lambda^2$
$I_{xT4}[f]$	$a_0 f_{-1.25} + a_1 f_{-0.25} + a_2 f_{0.75}$	$1, \sin(\lambda), \cos(\lambda)$
$I_{xT6}[f]$	$a_0 f_{-2.25} + a_1 f_{-1.25} + a_2 f_{-0.25} + a_3 f_{0.75} + a_4 f_{1.75}$	$1, \sin(\lambda), \cos(\lambda), \sin(2\lambda), \cos(2\lambda)$

(c) Discrete derivative (λ_0 is a midpoint)

Derivative	Expression	Functions such that $D_x[f](\lambda_0) = \partial_x f(\lambda_0)$
$D_{xP2}[f]$	$(a_0 f_{-0.5} - a_0 f_{0.5})/(a\cos(\varphi_0))$	$1, \lambda$
$D_{xP4}[f]$	$(a_1 f_{-1.5} + a_0 f_{-0.5} - a_0 f_{0.5} - a_1 f_{1.5})/(a\cos(\varphi_0))$	$1, \lambda, \lambda^2, \lambda^3$
$D_{xT4}[f]$	$(a_1 f_{-1.5} + a_0 f_{-0.5} - a_0 f_{0.5} - a_1 f_{1.5})/(a\cos(\varphi_0))$	$1, \sin(\lambda), \cos(\lambda)$
$D_{xT6}[f]$	$(a_2 f_{-2.5} + a_1 f_{-1.5} + a_0 f_{-0.5} - a_0 f_{0.5} - a_1 f_{1.5} - a_2 f_{2.5})/(a\cos(\varphi_0))$	$1, \sin(\lambda), \cos(\lambda), \sin(2\lambda), \cos(2\lambda)$

(d) Line quadrature between two midpoints ($L = [\lambda_{-0.5}, \lambda_{0.5}]$)

Quadrature	Expression	Functions such that $Q_x[f](L) = \int_\Gamma f$
$Q_{xP1}[f]$	$(a_0 f_0) a\cos(\varphi_0)$	$1, \lambda$
$Q_{xP3}[f]$	$(a_1 f_{-1} + a_0 f_0 + a_1 f_1) a\cos(\varphi_0)$	$1, \lambda, \lambda^2$
$Q_{xT3}[f]$	$(a_1 f_{-1} + a_0 f_0 + a_1 f_1) a\cos(\varphi_0)$	$1, \sin(\lambda), \cos(\lambda)$
$Q_{xT5}[f]$	$(a_2 f_{-2} + a_1 f_{-1} + a_0 f_0 + a_1 f_1 + a_2 f_2) a\cos(\varphi_0)$	$1, \sin(\lambda), \cos(\lambda), \sin(2\lambda), \cos(2\lambda)$

(e) Line quadrature between a quarter-point and a midpoint ($L = [\lambda_{0.25}, \lambda_{0.5}]$)

Quadrature	Expression	Functions such that $Q_x[f](L) = \int_\Gamma f$
$Q_{xP3}[f]$	$(a_0 f_{-1} + a_1 f_0 + a_2 f_1) a\cos(\varphi_0)$	$1, \lambda, \lambda^2$
$Q_{xT3}[f]$	$(a_0 f_{-1} + a_1 f_0 + a_2 f_1) a\cos(\varphi_0)$	$1, \sin(\lambda), \cos(\lambda)$
$Q_{xT5}[f]$	$(a_0 f_{-2} + a_1 f_{-1} + a_2 f_0 + a_3 f_1 + a_4 f_2) a\cos(\varphi_0)$	$1, \sin(\lambda), \cos(\lambda), \sin(2\lambda), \cos(2\lambda)$

Table 5
Expressions employed for zonal interpolations, derivatives, and line quadratures. Columns indicate the notation of each approximation, corresponding linear combination, and functions represented exactly.

This study was financed in part by the Coordenação de Aperfeiçoamento de Pessoal de Nível Superior, Brasil (CAPES), Finance Code 001, and also by Fundação de Amparo à Pesquisa do Estado de São Paulo (FAPESP), grant number 16/18445-7.

A. Definition of trigonometric zonal approximations

We will describe the approximations using the same notation for the points. Consider a sequence with J points uniformly spaced over a latitude line. Latitude is $\varphi = \varphi_0$ and the zonal angular distance is $\Delta\lambda = 2\pi/J$. At each situation, we will take a longitude λ_0 as reference. Each known value of the target function f will be denoted using a rational index. For instance, when λ_0 is a quarter-point, $f_{0.75}$ will designate the value of f at coordinates $\varphi = \varphi_0$ and $\lambda = \lambda_0 + 0.75\Delta\lambda$.

Table 5 describes the approximations considered for zonal interpolations, discrete derivatives, and line quadratures. Columns present each notation, linear combination, and the functions that will be exactly represented. The coefficients $a_0, a_1, \ldots$ are calculated to provide the exact value for the corresponding set of functions.

We will write the coefficients using the same letters at each expression, but they are independent. For instance, a_0 of I_{xP2} with midpoint may be different from a_0 of any other expression. The parameters of each approximation vary with φ_0 but are the same for any λ_0 in the same relative position on that row. For instance, interpolation I_{xT4} will have the same parameters for any λ_0 at a midpoint on the row with latitude φ_0.

Zonal discrete derivative over the sphere (with radius a) is the zonal component of gradient, $\partial_x f = (\partial f/\partial_\lambda)/(a\cos\varphi_0)$. Line quadratures depend on a longitude interval $L = [\lambda_{\text{west}}, \lambda_{\text{east}}]$. The spherical curve with $\varphi = \varphi_0$ and $\lambda \in L$ will be denoted by Γ. The line integral is $\int_\Gamma f = (a\cos\varphi_0)\int_L f(\lambda)d\lambda$.

References

D. L. Williamson, The evolution of dynamical cores for global atmospheric models, Journal of the Meteorological Society of Japan. Ser. II 85 (2007) 241–269.

A. Staniforth, J. Thuburn, Horizontal grids for global weather and climate prediction models: a review, Quarterly Journal of the Royal Meteorological Society 138 (2012) 1–26.

W. L. Gates, C. A. Riegel, A study of numerical errors in the integration of barotropic flow on a spherical grid, Journal of geophysical research 67 (1962) 773–784.

Y. Kurihara, Numerical integration of the primitive equations on a spherical grid, Monthly Weather Review 93 (1965) 399–415.

Y. Kurihara, J. L. Holloway Jr, Numerical integration of a nine-level global primitive equations model formulated by the box method, Monthly Weather Review 95 (1967) 509–530.

C. H. Dey, A note on global forecasting with the kurihara grid, Monthly Weather Review 97 (1969) 597–601.

F. G. Shuman, On certain truncation errors associated with spherical coordinates, Journal of Applied Meteorology 9 (1970) 564–570.

R. J. Purser, Accurate numerical differencing near a polar singularity of a skipped grid, Monthly weather review 116 (1988) 1067–1076.

G. Starius, A solution to the pole problem for the shallow water equations on a sphere, TWMS J. Pure Appl. Math 5 (2014) 152–170.

J.-G. Li, Shallow-water equations on a spherical multiple-cell grid, Quarterly Journal of the Royal Meteorological Society 144 (2018) 1–12.

P. Bénard, M. R. Glinton, Circumventing the pole problem of reduced lat–lon grids with local schemes. part i: Analysis and model formulation, Quarterly Journal of the Royal Meteorological Society 145 (2019) 1377–1391.

G. S. Goyman, V. V. Shashkin, Horizontal approximation schemes for the staggered reduced latitude-longitude grid, Journal of Computational Physics 434 (2021) 110234.

A. Arakawa, Computational design for long term integration of the equations of fluid motion: Two-dimensional incompressible flow, Part IJ Comput. Phys 1 (1966) 119–143.

F. Winninghoff, On the adjustment towards a geostrophic balance in a simple primitive equation model with application to the problems and objective analysis, Ph.D. thesis, Ph. D. thesis, University of California, 1968.

F. Mesinger, A. Arakawa, Numerical methods used in atmospheric models, volume 1, Global Atmospheric Research Program (GARP) (1976).

R. Sadourny, The dynamics of finite-difference models of the shallow-water equations, Journal of Atmospheric Sciences 32 (1975) 680–689.

D. Burridge, J. Haseler, A model for medium range weather forecasting: adiabatic formulation, European Centre for Medium-Range Weather Forecasts, 1977.

A. Arakawa, V. R. Lamb, A potential enstrophy and energy conserving scheme for the shallow water equations, Monthly Weather Review 109 (1981) 18–36.

T. D. Ringler, J. Thuburn, J. B. Klemp, W. C. Skamarock, A unified approach to energy conservation and potential vorticity dynamics for arbitrarily-structured c-grids, Journal of Computational Physics 229 (2010) 3065–3090.

H. Weller, J. Thuburn, C. J. Cotter, Computational modes and grid imprinting on five quasi-uniform spherical c grids, Monthly weather review 140 (2012) 2734–2755.

P. S. Peixoto, S. R. Barros, Analysis of grid imprinting on geodesic spherical icosahedral grids, Journal of Computational Physics 237 (2013) 61–78.

P. S. Peixoto, Accuracy analysis of mimetic finite volume operators on geodesic grids and a consistent alternative, Journal of Computational Physics 310 (2016) 127–160.

C. Eldred, Linear and nonlinear properties of numerical methods for the rotating shallow water equations, Ph.D. thesis, Colorado State University, 2015.

C. Eldred, D. Randall, Total energy and potential enstrophy conserving schemes for the shallow water equations using hamiltonian methods–part 1: Derivation and properties, Geoscientific Model Development 10 (2017) 791–810.

G. K. Vallis, Atmospheric and oceanic fluid dynamics, Cambridge University Press, 2006.

J. Pedlosky, et al., Geophysical fluid dynamics, volume 710, Springer, 1987.

D. L. Williamson, J. B. Drake, J. J. Hack, R. Jakob, P. N. Swarztrauber, A standard test set for numerical approximations to the shallow water equations in spherical geometry, Journal of Computational Physics 102 (1992) 211–224.

J. Thuburn, A. Staniforth, Conservation and linear rossby-mode dispersion on the spherical c grid, Monthly weather review 132 (2004) 641–653.

S. Malardel, N. Wedi, W. Deconinck, M. Diamantakis, C. Kuhnlein, G. Mozdzynski, M. Hamrud, P. Smolarkiewicz, A new grid for the ifs, ECMWF newsletter 146 (2016) 321.

D. R. Durran, Time discretization: Some basic approaches, in: Numerical Techniques for Global Atmospheric Models, Springer, 2011, pp. 75–104.

L. J. Wicker, W. C. Skamarock, Time-splitting methods for elastic models using forward time schemes, Monthly weather review 130 (2002) 2088–2097.

Q. Du, M. D. Gunzburger, L. Ju, Constrained centroidal voronoi tessellations for surfaces, SIAM Journal on Scientific Computing 24 (2003) 1488–1506.

R. Shapiro, Linear filtering, Mathematics of computation 29 (1975) 1094–1097.

C. Jablonowski, D. L. Williamson, The pros and cons of diffusion, filters and fixers in atmospheric general circulation models, Numerical techniques for global atmospheric models (2011) 381–493.

J. Galewsky, R. K. Scott, L. M. Polvani, An initial-value problem for testing numerical models of the global shallow-water equations, Tellus A: Dynamic Meteorology and Oceanography 56 (2004) 429–440.

P. S. Peixoto, J. Thuburn, M. J. Bell, Numerical instabilities of spherical shallow-water models considering small equivalent depths, Quarterly Journal of the Royal Meteorological Society 144 (2018) 156–171.

A. Hollingsworth, P. Kållberg, V. Renner, D. Burridge, An internal symmetric computational instability, Quarterly Journal of the Royal Meteorological Society 109 (1983) 417–428.